

Scattering Signatures of Bond-Dependent Magnetic Interactions

Joseph A. M. Paddison*

Materials Science and Technology Division, Oak Ridge National Laboratory, Oak Ridge, TN 37831, USA

Bond-dependent magnetic interactions can generate exotic topological states such as Kitaev and frustrated spin liquids. Experimentally determining the values of bond-dependent interactions in magnetic materials is a challenging but crucial problem. Here, I show that each symmetry-allowed nearest-neighbor interaction on triangular and honeycomb lattices has a distinct signature in paramagnetic neutron-diffraction data, and that such data actually contain sufficient information to determine the spin Hamiltonian unambiguously *via* unconstrained fits. Moreover, I show that bond-dependent interactions can often be extracted from powder-averaged data. These results facilitate experimental determination of the spin Hamiltonians of candidate topological materials.

The discovery and characterization of magnetic materials with topologically ordered ground states is an overarching goal of condensed-matter physics. Such materials have potential applications for topological quantum computation [1, 2], and are of fundamental interest because they can show entangled ground states whose excitations have fractional quantum numbers [3, 4]. Traditionally, the search for such states has concentrated on materials with isotropic (Heisenberg) magnetic interactions. However, the discovery of the celebrated Kitaev model [1, 5–7]—in which bond-dependent interactions generate topological spin-liquid ground states on the honeycomb lattice—has led to intense interest in materials with bond-dependent interactions [8–11]. Candidate honeycomb-lattice materials in which strong spin-orbit coupling drives bond-dependent interactions include α -RuCl₃ [12–16], YbCl₃ [17], NaNi₂BiO_{6- δ} [18], H₃LiIr₂O₆ [19, 20], Na₂IrO₃ [21–23], and α -Li₂IrO₃ [24, 25]. Bond-dependent interactions on the triangular lattice may promote the formation of quantum spin liquid states [26], with potential realizations including YbMgGaO₄ [27–30], NaYbS₂ [31, 32], and NaYbO₂ [33, 34].

Robust experimental determination of bond-dependent interactions is key to identifying the most promising topological materials. Yet, such interactions are challenging to measure; e.g., in the well-studied Kitaev candidate material α -RuCl₃, no clear consensus has been reached on the sign or magnitude of the Kitaev interaction, with experimental estimates ranging from -24 to $+7$ meV [35]. There are two main reasons for this difficulty. First, the spin Hamiltonian for triangular and honeycomb lattices contains four nearest-neighbor interactions [36], but most experiments are sensitive only to a subset of these. Second, current data-analysis approaches typically assume conventional long-range magnetic order—e.g., to model magnon spectra [13, 37–40]—but this is problematic because conventional magnetic ordering is not expected in topological states [4]. When long-range ordering does occur in candidate materials, it is often unclear if it is driven by the nearest-neighbor model itself or by perturbations to it, such as further-neighbor interactions or structural disorder [41–45].

In this Letter, I explore the extent to which bond-dependent interactions can be extracted from neutron-diffraction patterns measured in the *paramagnetic* phase, above any spin ordering or freezing temperature T_N . Such data show a continuous (dif-

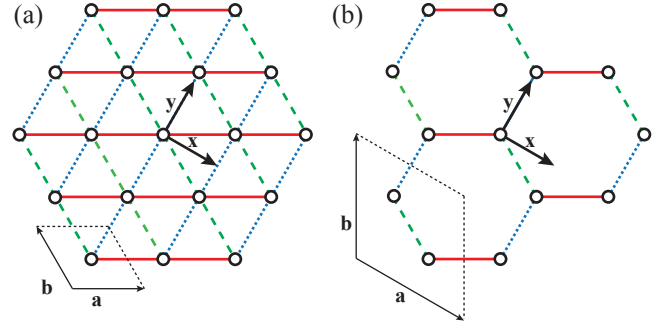


Figure 1. (a) Triangular and (b) honeycomb lattices. Spins are referred to Cartesian unit vectors \mathbf{x} , \mathbf{y} , and \mathbf{z} , where \mathbf{z} is directed out of the page. The conventional unit-cell vectors are \mathbf{a} , \mathbf{b} , and $\mathbf{c} \parallel \mathbf{z}$. The three types of bond are shown as solid red, dashed green, and dotted blue lines.

fuse) variation of the magnetic scattering intensity $I(\mathbf{Q})$ as a function of wavevector $\mathbf{Q} = ha^* + kb^* + lc^*$. I proceed by simulating $I(\mathbf{Q})$ data for a range of classical bond-dependent models (test cases) on triangular and honeycomb lattices. I show that $I(\mathbf{Q})$ contains distinctive signatures of the signs of bond-dependent interactions, which can be “read” directly from the data. I demonstrate that, in every test case, these interactions can be accurately determined *via* unconstrained fits to simulated $I(\mathbf{Q})$ data, and that this approach is robust to the level of statistical noise typical of real measurements. Perhaps most surprisingly, powder averaging $I(\mathbf{Q})$ does not entirely remove its sensitivity to bond-dependent interactions; consequently, the powder $I(Q = |\mathbf{Q}|)$ can constrain such interactions when single-crystal samples are unavailable.

The most general nearest-neighbor spin Hamiltonian allowed by threefold symmetry of the magnetic site has the same form for triangular and honeycomb lattices [46], and can be written

$$\begin{aligned} \mathcal{H} = \sum_{(i,j)} \{ & J_X (S_i^x S_j^x + S_i^y S_j^y) + J_Z S_i^z S_j^z \\ & + J_A [(S_i^x S_j^x - S_i^y S_j^y) \cos \phi_{ij} - (S_i^x S_j^y + S_i^y S_j^x) \sin \phi_{ij}] \\ & - J_B \sqrt{2} [(S_i^x S_j^z + S_i^z S_j^x) \cos \phi_{ij} + (S_i^y S_j^z + S_i^z S_j^y) \sin \phi_{ij}] \}, \end{aligned} \quad (1)$$

where superscript x , y , and z denote spin components with respect to the \mathbf{x} , \mathbf{y} , and \mathbf{z} axes shown in Fig. 1, and $\phi_{ij} \in$

* paddisonja@ornl.gov

$\{\frac{2\pi}{3}, -\frac{2\pi}{3}, 0\}$ for bonds colored red, green, and blue respectively in Fig. 1. The Hamiltonian contains four interactions, whose physical origin is typically superexchange between trigonally-distorted edge-sharing MO_6 octahedra [22]: J_X and J_Z describe a conventional XXZ model, while J_A and J_B are bond dependent. Several parameterizations of Eq. (1) are in use [47]; I follow the conventions of Ref. 36, which are similar to those applied to $YbMgGaO_4$ [27–30]. A different parameterization $\{J, K, \Gamma, \Gamma'\}$ is typically used for honeycomb systems [22, 36]. However, we will see that Eq. (1) has advantages for interpreting $I(\mathbf{Q})$ data.

I consider seven test cases with interaction parameters $\{J_X, J_Z, J_A, J_B\}$ (“ J ’s”) covering a range of interaction space: (i) the antiferromagnetic (AF) Heisenberg model, $\{1, 1, 0, 0\}$; (ii) the AF Ising model, $\{0, 1, 0, 0\}$; (iii, iv) the AF Heisenberg model with $J_A = +1$ and -1 ($\equiv \bar{1}$), respectively; (v, vi) the AF Heisenberg model with $J_B = +\frac{3}{4}$ and $-\frac{3}{4}$, respectively; and (vii) the ferromagnetic Kitaev model, $\{\frac{2}{3}, \frac{2}{3}, \frac{2}{3}, \frac{2}{3}\}$, which corresponds to $\{J, K, \Gamma, \Gamma'\} = \{0, \bar{2}, 0, 0\}$. Test cases (i) and (ii) are not bond-dependent and are included for comparison; (iii)–(vi) explore the effect of changing signs of bond-dependent terms and are potentially relevant to $YbMgGaO_4$ [27–30]; and (vii) explores the Kitaev limit potentially relevant to α - $RuCl_3$ [13–16]. For each test case, I performed classical Monte Carlo (MC) simulations of Eq. (1) with spin length $|\mathbf{S}| = 1$ [47]. The simulation temperature $T = 2$ (in the same units as the J ’s) for (iii)–(vii) on the triangular lattice, and $T = 1$ otherwise, which is well above T_N in all cases. The energy-integrated magnetic neutron-diffraction intensity

$$I(\mathbf{Q}) \propto [f(Q)]^2 \sum_{i,j,\alpha,\beta} p_{\alpha\beta} \langle S_i^\alpha S_j^\beta \rangle e^{i\mathbf{Q}\cdot\mathbf{r}_{ij}}, \quad (2)$$

where $\alpha, \beta \in \{x, y, z\}$ denote spin components, \mathbf{r}_{ij} is the vector connecting spins i and j , $f(Q)$ denotes an arbitrary magnetic form factor (Yb^{3+}) [48], and

$$p_{\alpha\beta} \equiv \delta_{\alpha\beta} - Q_\alpha Q_\beta / Q^2 \quad (3)$$

is the projection factor [49–51], which arises because neutrons only “see” spin components perpendicular to \mathbf{Q} , and couples spin and spatial degrees of freedom. Eq. (3) is key to magnetic crystallography because it usually allows the absolute spin structure to be solved from $T < T_N$ neutron-diffraction data [52]; I will show that it also allows bond-dependent interactions to be inferred from $T > T_N$ neutron-diffraction data.

Fig. 2 shows the single-crystal $I(\mathbf{Q})$ and powder $I(Q)$ for all test cases. Two orthogonal single-crystal planes are shown: $(hk0)$, and either $(h0l)$ for the triangular lattice or (hhl) for the honeycomb lattice. Our first key result is that $I(\mathbf{Q})$ is qualitatively different in each case. In particular, it is strongly affected by changing the sign of J_A or J_B : this is significant because other experiments (e.g., magnon spectra [13, 37–39]) are usually insensitive to at least one of these signs. Moreover, differences are evident in the $(h0l)$ or (hhl) plane. These differences do not arise from inter-layer interactions—absent in all test cases—but instead from the projection factor, as I now discuss for each test case. (i) The Heisenberg diffraction pattern is identical in every Brillouin zone, except for the trivial

decrease of intensity with $f(Q)$. This is because all diagonal correlators $\langle S_i^\alpha S_j^\alpha \rangle$ are equal and all off-diagonal correlators $\langle S_i^\alpha S_j^\beta \rangle$ are zero; hence $\langle p_{\alpha\alpha} \rangle = 2/3$ is independent of \mathbf{Q} . (ii) The Ising diffraction pattern is identical in every Brillouin zone in the $(hk0)$ plane, but shows further \mathbf{Q} -dependence in the perpendicular plane. This is because the intensity is dominated by $p_{zz} \langle S_i^z S_j^z \rangle = (1 - Q_z^2/Q^2) \langle S_i^z S_j^z \rangle$ terms. (iii, iv) Nonzero J_A causes nontrivial \mathbf{Q} -dependence in both planes; this is because it drives nonzero $\langle S_i^x S_j^x \rangle$ and $\langle S_i^y S_j^y \rangle$ correlators, so that terms like $p_{xy} \langle S_i^x S_j^y \rangle = -Q_x Q_y \langle S_i^x S_j^y \rangle / Q^2$ contribute to $I(\mathbf{Q})$. (v, vi) Nonzero J_B also causes nontrivial \mathbf{Q} -dependence in both planes, but unlike the previous cases, $I(hkl) \neq I(hk\bar{l})$. This is because nonzero J_B lowers the hexagonal symmetry of the previous models to trigonal [36], yielding nonzero terms like $p_{xz} \langle S_i^x S_j^z \rangle$ and $p_{yz} \langle S_i^y S_j^z \rangle$ that change sign under either $(hkl) \rightarrow (hk\bar{l})$ or $S_i^z \rightarrow -S_i^z$ for all S^z . Since the latter is equivalent to $J_B \rightarrow -J_B$ in Eq. (1), both $(hkl) \rightarrow (hk\bar{l})$ and $J_B \rightarrow -J_B$ have the same effect on $I(\mathbf{Q})$. These results follow from basic properties of Eqs. (1)–(3) that apply for quantum as well as classical systems, and show that each interaction has a different effect on $I(\mathbf{Q})$. They therefore allow the dominant interactions to be identified by inspection of diffraction data.

I now obtain a field theory that explains the modulation of $I(\mathbf{Q})$. I employ the Onsager reaction-field (MFO) method [53, 54] previously shown to give accurate results for Heisenberg models [55–60]. The Fourier transform of the interactions $J_{ij}^{\alpha\beta}(\mathbf{Q}) \equiv -\sum_{\mathbf{R}} J_{ij}^{\alpha\beta}(\mathbf{R}) e^{-i\mathbf{Q}\cdot\mathbf{R}}$, where $J_{ij}^{\alpha\beta}(\mathbf{R})$ is the coefficient of $S_i^\alpha S_j^\beta$ in Eq. (1) for sites i and j separated by a lattice vector \mathbf{R} . The $J_{ij}^{\alpha\beta}(\mathbf{Q})$ are elements of a $3N \times 3N$ interaction matrix, where N is the number of sites in the unit cell ($N = 1$ for triangular, $N = 2$ for honeycomb). For the triangular lattice, the interaction matrix

$$\mathbf{J}(\mathbf{Q}) = - \begin{pmatrix} aJ_X + bJ_A & cJ_A & -\sqrt{2}bJ_B \\ cJ_A & aJ_X - bJ_A & \sqrt{2}cJ_B \\ -\sqrt{2}bJ_B & \sqrt{2}cJ_B & aJ_Z \end{pmatrix}, \quad (4)$$

where $a = 2[\cos(h+k) + \cosh h + \cos k]$, $b = 2\cos(h+k) - \cosh h - \cos k$, and $c = \sqrt{3}(\cos k - \cosh h)$. For the honeycomb lattice, the interaction matrix

$$\mathbf{J}_h(\mathbf{Q}) = \begin{pmatrix} 0 & \mathbf{J} \\ \mathbf{J}^* & 0 \end{pmatrix}, \quad (5)$$

where a , b , and c in Eq. (4) are replaced by $a_h = 1 + e^{2\pi i h} + e^{2\pi i k}$, $b_h = e^{2\pi i k} - (1 + e^{2\pi i h})/2$, and $c_h = \sqrt{3}(1 - e^{2\pi i h})/2$, respectively. Diagonalizing the interaction matrix at each \mathbf{Q} yields its eigenvalues λ_μ and eigenvector components $U_\mu^{\alpha,i}$, where μ labels the $3N$ eigenmodes and i labels sites at positions \mathbf{r}_i in the unit cell. The $T > T_N$ scattering intensity in the reaction-field approximation is given by

$$I_{\text{MFO}}(\mathbf{Q}) \propto \frac{[f(Q)]^2}{3N} \sum_{\mu=1}^{3N} \frac{|\mathbf{s}_\mu(\mathbf{Q})|^2}{1 - \chi_0(\lambda_\mu(\mathbf{Q}) - \lambda)}, \quad (6)$$

where $\chi_0 = 1/3T$ is the Curie susceptibility, and $\mathbf{s}_\mu(\mathbf{Q}) = \sum_{i,\alpha} (\hat{\mathbf{n}}_\alpha - \mathbf{Q} \hat{\mathbf{n}}_\alpha \cdot \mathbf{Q} / Q^2) U_\mu^{\alpha,i} e^{i\mathbf{Q}\cdot\mathbf{r}_i}$ with $\hat{\mathbf{n}}_\alpha \in \{\mathbf{x}, \mathbf{y}, \mathbf{z}\}$. Eq. (6)

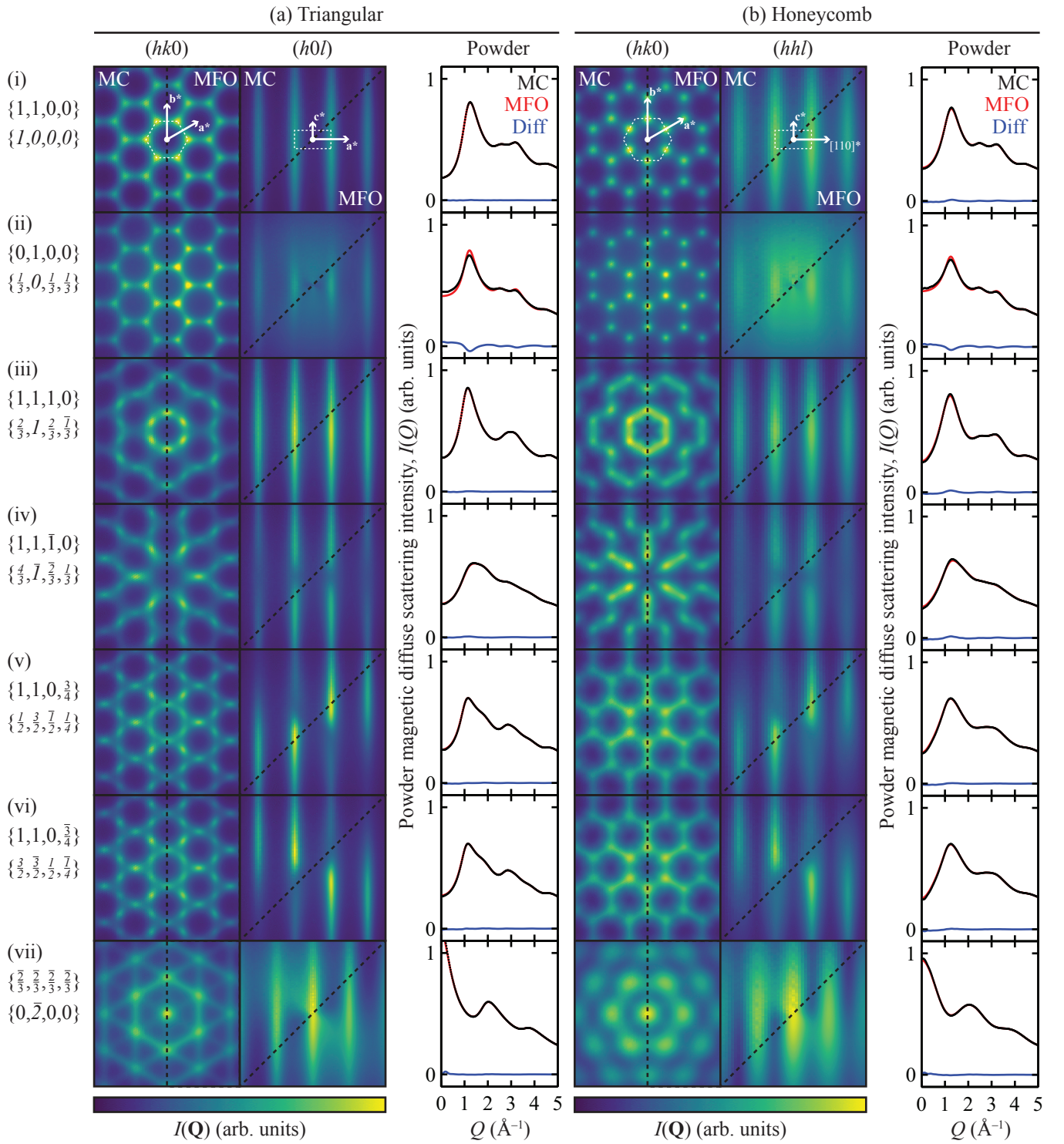


Figure 2. Simulated neutron-diffraction patterns in the paramagnetic phase for test cases (i)–(vii) discussed in the text. The interaction parameters for each model are shown left, with $\{J_X, J_Z, J_A, J_B\}$ in roman type above the corresponding $\{J, K, \Gamma, \Gamma'\}$ in italics. Column (a) shows calculations for the triangular lattice (left to right: $(hk0)$, $(h0l)$, and powder diffraction patterns) and column (b) shows calculations for the honeycomb lattice (left to right: $(hk0)$, (hhl) , and powder diffraction patterns). Results for Monte Carlo (MC) and reaction-field (MFO) approximations are shown separated by dashed black lines, as labeled on the top panels. For powder patterns, MC results are shown as black circles; MFO results as red lines; and difference (MC–MFO) as blue lines. All powder patterns are shown on the same intensity scale. For single-crystal patterns, reciprocal-lattice vectors \mathbf{a}^* , \mathbf{b}^* , and \mathbf{c}^* are labeled in the top panels, and the first Brillouin zone is shown as a white dashed line. Both single-crystal planes are shown on the same intensity scale for each test case except honeycomb (i) and (ii), for which the intensity scale is doubled in the (hhl) plane for clarity. In all calculations, the triangular unit cell has dimensions $|\mathbf{a}| = |\mathbf{b}| = 3.464 \text{ \AA}$, $|\mathbf{c}| = 6.0 \text{ \AA}$, and the honeycomb unit cell has dimensions $|\mathbf{a}| = |\mathbf{b}| = |\mathbf{c}| = 6.0 \text{ \AA}$.

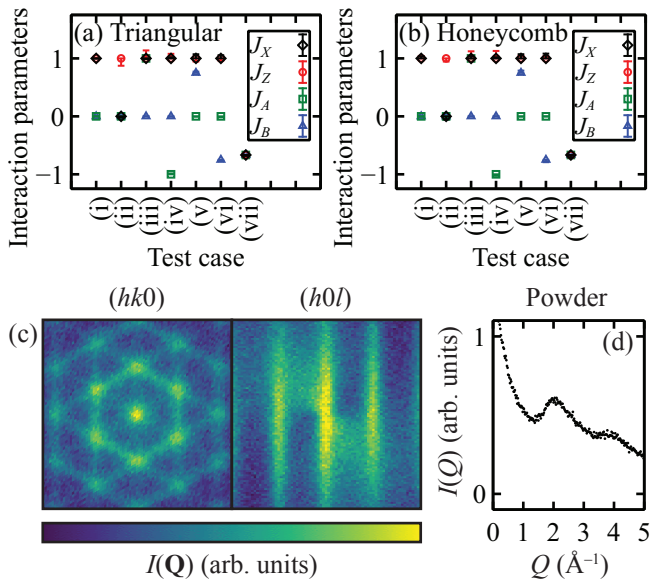


Figure 3. Values of the interaction parameters for test cases (i)–(vii) for (a) triangular and (b) honeycomb lattices. In each case, J_X is shown as black diamonds, J_Z as red circles, J_A as green squares, and J_B as blue triangles. Error bars indicate values obtained from unconstrained fits of all four parameters to the two single-crystal $I(\mathbf{Q})$ planes shown in Fig. 2. (c) Simulated “noisy” single-crystal data $I(\mathbf{Q})$ with 5% error bars. (d) Simulated “noisy” powder $I(Q)$ data with 1% error bars. Panels (c) and (d) are shown for the Kitaev model on the triangular lattice (test case (vii)).

is identical to the mean-field expression [61] except for the reaction field λ , which is determined self-consistently by requiring that $\sum_{\mu, \mathbf{q}} [1 - \chi_0(\lambda_{\mu}(\mathbf{q}) - \lambda)]^{-1} = 3N_{\mathbf{q}}$ for a grid of $N_{\mathbf{q}} = 40^3$ wavevectors in the Brillouin zone. Fig. 2 compares the single-crystal $I(\mathbf{Q})$ and powder $I(Q)$ from reaction-field theory with the accurate MC results. The agreement is very good in all cases; only in the Ising case are subtle differences evident [Fig. 2]. The success of reaction-field theory for bond-dependent interactions is remarkable given its simplicity.

The sensitivity of $I(\mathbf{Q})$ to bond-dependent interactions suggests that it may be possible to solve the inverse problem—to infer the interaction values from $I(\mathbf{Q})$ data. To test this possibility, I performed unconstrained fits of the four J ’s for each test case, using the MC scattering planes shown in Fig. 2 as input “data”. In the fits, $I(\mathbf{Q})$ was calculated in the reaction-field approximation because it is computationally efficient and free from statistical noise. The BFGS nonlinear least-squares algorithm in the MINUIT program [62] was used to minimize the sum of squared residuals χ^2 . If the J ’s are fully determined by the data, a fit should converge to a global minimum χ_{\min}^2 with J ’s close to the correct ones, provided the initial J ’s are sufficiently close to optimal. Conversely, if the J ’s are underdetermined, a fit will either fail, or converge to different low-lying false minima depending on initial J ’s. To determine which scenario applies, I performed 50 separate fits initialized with different J ’s randomly distributed in the range $\{-0.5 : 0.5\}$. In every test case, the fits identified a unique optimal solution with nearly correct J ’s, and convergence was

achieved from nearly all (98%) of the initial parameter sets. Fig. 3 shows the systematic error in the optimal J ’s due to the inaccuracy of the reaction-field approximation. This error is usually small, and the worst-case error is 0.14 in J_Z . These results show that bond-dependent interactions can be reliably extracted from ideal $I(\mathbf{Q})$ data.

Diffraction experiments inevitably produce data that are to some extent imperfect. I now discuss the effects of common data limitations. First, I adulterated the single-crystal data with random noise drawn from a normal distribution with σ equal to 5% of the maximum intensity (“5% error bars”). Representative noisy data are shown in Fig. 3(c). In subsequent fits, an intensity scale factor was included as a free parameter, as required if data are not normalized on an absolute intensity scale. The optimal solution was again identified in every test case, and no low-lying false minima—defined as solutions with $\chi^2 < \chi_{\min}^2 + 15$, where this condition reflects the 99% confidence interval for five parameters [63]—were found. Hence, bond-dependent interactions can still be reliably extracted from noisy and unnormalized $I(\mathbf{Q})$ data.

As a more challenging test, I considered *powder-averaged* noisy data $I(Q)$ with 1% error bars [Fig. 3(d)]. On the one hand, powder averaging causes much information loss. In particular, powder data cannot distinguish $\pm J_B$, because $J_B \rightarrow -J_B$ is equivalent to $(hkl) \rightarrow (h\bar{k}l)$; I therefore consider test cases (v, vi) together. On the other hand, $I(Q)$ differs for the other test cases and hence retains some sensitivity to bond-dependent interactions [Fig. 2]. Remarkably, fits of the four J ’s to noisy $I(Q)$ data yielded a unique optimal solution with nearly correct J ’s in 10 out of 12 test cases, for which no low-lying false minima with $\chi^2 < \chi_{\min}^2 + 15$ were found. In the remaining cases—(iii) and (v, vi) for the triangular lattice—two different solutions were identified with nearly the same χ^2 . Parameter uncertainties were also increased compared to single-crystal fits [47]. Despite these limitations, the ability of powder fits to identify a small number of candidate models suggests that $I(Q)$ can provide a “fingerprint” of bond-dependent interactions—a compact data set that contains most of the discriminating information.

These results show that bond-dependent interactions on triangular and honeycomb lattices have signatures in diffuse neutron-diffraction data at $T > T_N$ that enable estimation of the interactions *via* unconstrained fits. This unexpected sensitivity is mainly due to the projection factor, Eq. (3); hence, it is important to measure $I(\mathbf{Q})$ outside the $(hk0)$ plane where this factor is significant, and to include it in calculations. Our methodology is generally applicable and employs conventional least-squares optimization [59], providing a robust and computationally-efficient alternative to machine-learning-based approaches [64], as well as to interaction-independent approaches such as reverse Monte Carlo refinement [65] and pair-distribution-function analysis [66]. A limitation is that quantum effects that redistribute scattering intensity [67, 68] are not included: this may cause inaccuracy in fitted interaction values, but does not affect the sensitivity to interaction signs, which arises from general considerations. Moreover, a fit typically requires only a few hundred $I(\mathbf{Q})$ calculations for convergence—taking ~ 60 s to fit to $\sim 10^4$ data points on a

laptop—so that replacement of classical calculations by more expensive quantum calculations is feasible. Our results are unaffected by the layer stacking sequence provided that inter-layer interactions can be neglected above T_N —a useful feature because of the prevalence of stacking faults in quasi-2D materials [69]. Perhaps our most surprising result is that powder-averaged $I(Q)$ data can provide a “fingerprint” of the bond-dependent interactions. These results promise to accelerate experimental determination of the spin Hamiltonians of candidate topological materials, such as in the emerging field of “topology by design” metal-organic frameworks [70].

I am grateful to Xiaojian Bai (ORNL), Andrew Christianson (ORNL), Seung-Hwan Do (ORNL), Mechthild Enderle (ILL), Andrew Goodwin (Oxford), Pontus Laurell (ORNL), Martin Mourigal (Georgia Tech), Allen Scheie (ORNL), Ross Stewart (ISIS), and Alan Tennant (ORNL) for valuable discussions. This work was supported by ORNL LDRD 10004, and by the U.S. Department of Energy, Office of Science, Basic Energy Sciences, Materials Sciences and Engineering Division. I acknowledge a Junior Research Fellowship from Churchill College, University of Cambridge, during which computer programs underlying this work were written.

-
- [1] A. Kitaev, *Ann. Phys.* **303**, 2 (2003).
- [2] C. Nayak, S. H. Simon, A. Stern, M. Freedman, S. Das Sarma, *Rev. Mod. Phys.* **80**, 1083 (2008).
- [3] H. Takagi, T. Takayama, G. Jackeli, G. Khaliullin, S. E. Nagler, *Nat. Rev. Phys.* **1**, 264 (2019).
- [4] C. Broholm, *et al.*, *Science* **367** (2020).
- [5] G. Baskaran, S. Mandal, R. Shankar, *Phys. Rev. Lett.* **98**, 247201 (2007).
- [6] M. Hermanns, I. Kimchi, J. Knolle, *Ann. Rev. Condens. Matter Phys.* **9**, 17 (2018).
- [7] I. Rousochatzakis, Y. Sizyuk, N. B. Perkins, *Nature Communications* **9**, 1575 (2018).
- [8] G. Jackeli, G. Khaliullin, *Phys. Rev. Lett.* **102**, 017205 (2009).
- [9] J. Chaloupka, G. Jackeli, G. Khaliullin, *Phys. Rev. Lett.* **105**, 027204 (2010).
- [10] S. M. Winter, *et al.*, *J. Phys.: Condens. Matter* **29**, 493002 (2017).
- [11] R. Sano, Y. Kato, Y. Motome, *Phys. Rev. B* **97**, 014408 (2018).
- [12] K. W. Plumb, *et al.*, *Phys. Rev. B* **90**, 041112 (2014).
- [13] A. Banerjee, *et al.*, *Nat. Mater.* **15**, 733 (2016).
- [14] S.-H. Do, *et al.*, *Nat. Phys.* **13**, 1079 (2017).
- [15] A. Banerjee, *et al.*, *Science* **356**, 1055 (2017).
- [16] S. M. Winter, *et al.*, *Nature Communications* **8**, 1152 (2017).
- [17] G. Sala, *et al.*, *Phys. Rev. B* **100**, 180406 (2019).
- [18] A. Scheie, *et al.*, *Phys. Rev. B* **100**, 214421 (2019).
- [19] K. Kitagawa, *et al.*, *Nature* **554**, 341 (2018).
- [20] R. Yadav, *et al.*, *Phys. Rev. Lett.* **121**, 197203 (2018).
- [21] Y. Singh, *et al.*, *Phys. Rev. Lett.* **108**, 127203 (2012).
- [22] J. G. Rau, E. K.-H. Lee, H.-Y. Kee, *Phys. Rev. Lett.* **112**, 077204 (2014).
- [23] S. Hwan Chun, *et al.*, *Nat. Phys.* **11**, 462 (2015).
- [24] S. C. Williams, *et al.*, *Phys. Rev. B* **93**, 195158 (2016).
- [25] S. Choi, *et al.*, *Phys. Rev. B* **99**, 054426 (2019).
- [26] Z. Zhu, P. A. Maksimov, S. R. White, A. L. Chernyshev, *Phys. Rev. Lett.* **120**, 207203 (2018).
- [27] Y. Li, *et al.*, *Phys. Rev. Lett.* **115**, 167203 (2015).
- [28] Y. Shen, *et al.*, *Nature* **540**, 559 (2016).
- [29] J. A. M. Paddison, *et al.*, *Nat. Phys.* **13**, 117 (2017).
- [30] Y. Li, *et al.*, *Nat. Commun.* **8**, 15814 (2017).
- [31] M. Baenitz, *et al.*, *Phys. Rev. B* **98**, 220409 (2018).
- [32] R. Sarkar, *et al.*, *Phys. Rev. B* **100**, 241116 (2019).
- [33] M. M. Bordelon, *et al.*, *Nat. Phys.* **15**, 1058 (2019).
- [34] L. Ding, *et al.*, *Phys. Rev. B* **100**, 144432 (2019).
- [35] P. Laurell, S. Okamoto, *npj Quantum Mater.* **5**, 2 (2020).
- [36] J. Chaloupka, G. Khaliullin, *Phys. Rev. B* **92**, 024413 (2015).
- [37] K. Ran, *et al.*, *Phys. Rev. Lett.* **118**, 107203 (2017).
- [38] I. O. Ozel, *et al.*, *Phys. Rev. B* **100**, 085108 (2019).
- [39] X. Zhang, *et al.*, *Phys. Rev. X* **8**, 031001 (2018).
- [40] K. A. Ross, L. Savary, B. D. Gaulin, L. Balents, *Phys. Rev. X* **1**, 021002 (2011).
- [41] P. Lampen-Kelley, *et al.*, *Phys. Rev. Lett.* **119**, 237203 (2017).
- [42] Z. Zhu, P. A. Maksimov, S. R. White, A. L. Chernyshev, *Phys. Rev. Lett.* **119**, 157201 (2017).
- [43] Y. Li, *et al.*, *Phys. Rev. Lett.* **118**, 107202 (2017).
- [44] R. Sarkar, *et al.*, *Phys. Rev. B* **101**, 081101 (2020).
- [45] S. M. Winter, Y. Li, H. O. Jeschke, R. Valentí, *Phys. Rev. B* **93**, 214431 (2016).
- [46] J. G. Rau, M. J. P. Gingras, *Phys. Rev. B* **98**, 054408 (2018).
- [47] See supplementary information [URL will be inserted by publisher] for relations between Hamiltonian parameterizations, details of Monte Carlo simulations, and fit statistics.
- [48] P. J. Brown, *International Tables for Crystallography* (Kluwer Academic Publishers, Dordrecht, 2004), vol. C, chap. Magnetic Form Factors, pp. 454–460.
- [49] S. W. Lovesey, *Theory of Neutron Scattering from Condensed Matter: Polarization Effects and Magnetic Scattering*, vol. 2 (Oxford University Press, Oxford, 1987).
- [50] O. Halpern, M. H. Johnson, *Phys. Rev.* **55**, 898 (1939).
- [51] J. A. M. Paddison, *Acta Crystallogr. A* **75**, 14 (2019).
- [52] G. Shirane, *Acta Crystallogr.* **12**, 282 (1959).
- [53] R. Brout, H. Thomas, *Physique Physique Fizika* **3**, 317 (1967).
- [54] G. M. Wysin, *Phys. Rev. B* **62**, 3251 (2000).
- [55] D. E. Logan, Y. H. Szczech, M. A. Tusch, *Europhys. Lett. (EPL)* **30**, 307 (1995).
- [56] M. P. Eastwood, D. E. Logan, *Phys. Rev. B* **52**, 9455 (1995).
- [57] D. Hohlwein, J.-U. Hoffmann, R. Schneider, *Phys. Rev. B* **68**, 140408 (2003).
- [58] P. H. Conlon, J. T. Chalker, *Phys. Rev. B* **81**, 224413 (2010).
- [59] X. Bai, *et al.*, *Phys. Rev. Lett.* **122**, 097201 (2019).
- [60] K. W. Plumb, *et al.*, *Nat. Phys.* **15**, 54 (2019).
- [61] M. Enjalran, M. J. P. Gingras, *Phys. Rev. B* **70**, 174426 (2004).
- [62] F. James, M. Roos, *Comp. Phys. Commun.* **10**, 343 (1975).
- [63] F. James, *MINUIT Function Minimization and Error Analysis: Reference Manual Version 94.1*, CERN (1994).
- [64] A. M. Samarakoon, *et al.*, *Nat. Commun.* **11**, 892 (2020).
- [65] J. A. M. Paddison, A. L. Goodwin, *Phys. Rev. Lett.* **108**, 017204 (2012).
- [66] B. A. Frandsen, X. Yang, S. J. L. Billinge, *Acta Crystallogr. A* **70**, 3 (2014).
- [67] M. Mourigal, W. T. Fuhrman, A. L. Chernyshev, M. E. Zhitomirsky, *Phys. Rev. B* **88**, 094407 (2013).
- [68] A. M. Samarakoon, *et al.*, *Phys. Rev. B* **96**, 134408 (2017).
- [69] R. D. Johnson, *et al.*, *Phys. Rev. B* **92**, 235119 (2015).
- [70] M. G. Yamada, H. Fujita, M. Oshikawa, *Phys. Rev. Lett.* **119**, 057202 (2017).